

Article

# Phase Separation Prevents the Synthesis of $\text{VBi}_2\text{Te}_4$ by Molecular Beam Epitaxy

Marieke Altena <sup>\*</sup>, Thies Jansen <sup>\*</sup>, Martina Tsvetanova and Alexander Brinkman

MESA+ Institute for Nanotechnology, University of Twente, 7500 AE Enschede, The Netherlands

<sup>\*</sup> Correspondence: m.w.altena@utwente.nl (M.A.); t.jansen@utwente.nl (T.J.)

**Abstract:** Intrinsic magnetic topological insulators (IMTIs) have a non-trivial band topology in combination with magnetic order. This potentially leads to fascinating states of matter, such as quantum anomalous Hall (QAH) insulators and axion insulators. One of the theoretically predicted IMTIs is  $\text{VBi}_2\text{Te}_4$ , but experimental evidence of this material is lacking so far. Here, we report on our attempts to synthesise  $\text{VBi}_2\text{Te}_4$  by molecular beam epitaxy (MBE). X-ray diffraction reveals that in the thermodynamic phase space reachable by MBE, there is no region where  $\text{VBi}_2\text{Te}_4$  is stably synthesised. Moreover, scanning transmission electron microscopy shows a clear phase separation to  $\text{Bi}_2\text{Te}_3$  and  $\text{VTe}_2$  instead of the formation of  $\text{VBi}_2\text{Te}_4$ . We suggest the phase instability to be due to either the large lattice mismatch between  $\text{VTe}_2$  and  $\text{Bi}_2\text{Te}_3$  or the unfavourable valence state of vanadium.

**Keywords:** molecular beam epitaxy;  $\text{VBi}_2\text{Te}_4$ ; magnetic topological insulator; phase separation; crystal growth

## 1. Introduction

Over the last decade, the introduction of magnetic order into 3D topological insulators (TIs) has attracted considerable interest. The bandstructure of a TI is characterised by a gapless Dirac cone at the surface, resulting in conducting surface states that are protected by time-reversal symmetry [1]. Magnetism breaks the time-reversal symmetry via exchange interaction and opens a gap in the conducting surface states [1–4]. This exchange gap can give rise to interesting phases such as the quantum anomalous Hall (QAH) state [2,5–11] and the axion insulating state [12–15].

To introduce magnetism into TIs, the following methods are currently used [16]: doping magnetic ions into the TI [6,7,11,17], bringing the TI in proximity with ferromagnetic materials [10,16,18–20] and incorporating intrinsic magnetic moments in the crystal structure, which results in an intrinsic magnetic topological insulator (IMTI) [8,9,14,21,22]. All three methods are successful in realising the QAH state; however, with the former two methods the temperatures at which this state arises is very low in the light of applications. It is interesting to compare the temperature at which the QAH effect is observed to the Curie temperature ( $T_C$ ) of the materials. Remarkably, the temperatures for observing the QAH effect are an order of magnitude smaller than  $T_C$  [16]. The explanation for this difference in temperature depends on the method used to introduce the magnetism. In the magnetically doped system, the high level of disorder caused by the random distribution of magnetic dopants may reduce the effective exchange gap [16], form a conducting bulk or create regions without ferromagnetic ordering [11]. In the magnetic proximity system, the sensitivity to the interface between the TI and the magnetic material is the main problem [14].

These challenges are overcome in IMTIs because in these materials the magnetic moment is intrinsically embedded in the unit cell. In 2019, Li et al. [9] theoretically predicted a class of materials acting as IMTIs, called the MBT family (M = transition-metal or rare-earth element, B = Bi or Sb and T = Te or Se). The materials in the MBT family



**Citation:** Altena, M.; Jansen, T.; Tsvetanova, M.; Brinkman, A. Phase Separation Prevents the Synthesis of  $\text{VBi}_2\text{Te}_4$  by Molecular Beam Epitaxy. *Nanomaterials* **2024**, *14*, 87. <https://doi.org/10.3390/nano14010087>

Academic Editor: Meiwen Cao

Received: 24 November 2023

Revised: 17 December 2023

Accepted: 26 December 2023

Published: 28 December 2023



**Copyright:** © 2023 by the authors. Licensee MDPI, Basel, Switzerland. This article is an open access article distributed under the terms and conditions of the Creative Commons Attribution (CC BY) license (<https://creativecommons.org/licenses/by/4.0/>).

have the same crystal structure, but their behaviour differs depending on the magnetic element (transition-metal or rare-earth element, M) in the MBT structure. The unit cell of the MBT family can be viewed as the unit cell of the well studied family of  $\text{Bi}_2\text{Te}_3$  TIs, with a structural intercalated layer containing a magnetic element. The addition of magnetism within the unit cell results in periodic magnetic layers, which results in a large magnetic exchange gap [9,21]. A representative material of the MBT family is  $\text{MnBi}_2\text{Te}_4$ , for which the crystal structure is shown in Figure 1a. Like other materials in the MBT family, it crystallises in the  $\bar{R}3m$  space group with a rhombohedral structure. Each monolayer has a triangular lattice with ABC stacking along the out-of-plane direction. A monolayer is structured as a septuple layer (SL) with T-B-T-M-T-B-T stacking and a Van der Waals (VdW) gap separates consecutive SLs. The Mn atoms introduce a magnetic moment of  $5 \mu\text{B}$  per atom with an out-of-plane easy axis [9]. The exchange coupling within a single SL ( $J_{\parallel}$ ) is ferromagnetic (FM), while the coupling between consecutive SLs ( $J_{\perp}$ ) is antiferromagnetic (AFM) [9,23–25]. In these VdW materials, the  $J_{\parallel}$  is much stronger than  $J_{\perp}$  [23,26].

Another potential member of the MBT family of IMTIs is the theoretically predicted  $\text{VBi}_2\text{Te}_4$  [9]. In contrast to  $\text{MnBi}_2\text{Te}_4$ ,  $\text{VBi}_2\text{Te}_4$  has a predicted in-plane easy axis (Figure 1b), the V-atoms introduce a magnetic moment of  $3 \mu\text{B}$  per atom [9,26] and a stronger  $J_{\perp}$  is expected in  $\text{VBi}_2\text{Te}_4$  leading to a higher  $T_C$  [26]. The latter could potentially result in a higher temperature at which topological phases such as QAH can be observed, opening up possibilities for applications. However, to the best of our knowledge, no experimental evidence of  $\text{VBi}_2\text{Te}_4$  has been published so far.

In this work, we report on a structural MBE study to synthesise  $\text{VBi}_2\text{Te}_4$ . The crystal structure of the films was analysed by X-ray diffraction (XRD), scanning transmission electron microscopy (STEM) and energy dispersive diffraction (EDX), which are suitable techniques to detect the presence of the SL structure of  $\text{VBi}_2\text{Te}_4$ . The surface morphology of the films was characterised by reflective high energy electron diffraction (RHEED) and atomic force microscopy (AFM). The analysis of the crystal structure indicates a phase separation to  $\text{Bi}_2\text{Te}_3$  and  $\text{VTe}_2$  instead of the SL structure of  $\text{VBi}_2\text{Te}_4$ . This observation suggests  $\text{VBi}_2\text{Te}_4$  to be unstable in the deposition conditions of MBE.

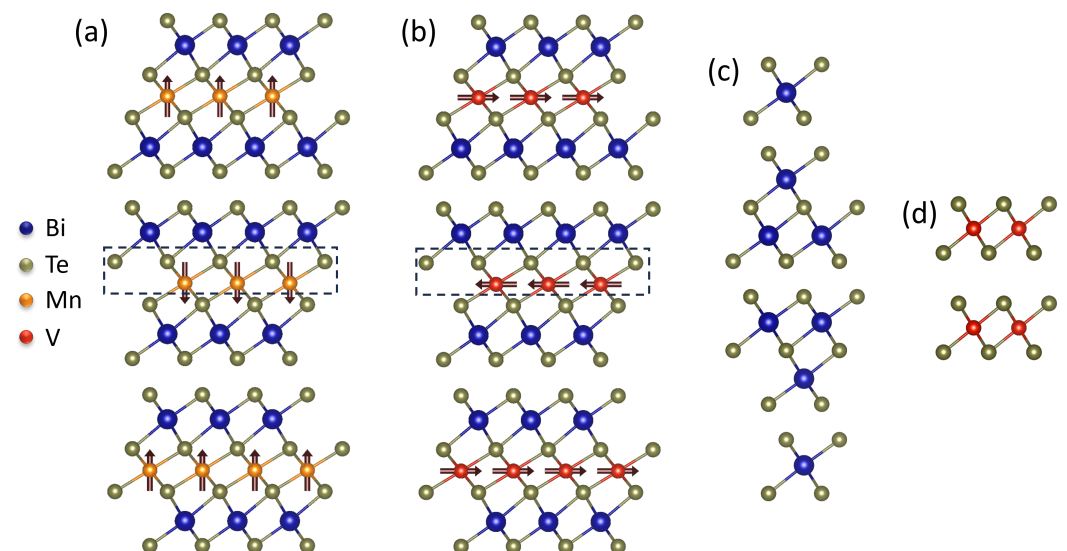


**Figure 1.** (a)  $\text{MnBi}_2\text{Te}_4$  and (b)  $\text{VBi}_2\text{Te}_4$  have a unit cell structured as SLs separated by a VdW gap. The dashed boxes indicate the relative intercalated layers of MnTe and VTe in  $\text{Bi}_2\text{Te}_3$ .  $J_{\parallel}$  is FM with either an (a) out-of-plane or (b) in-plane easy axis.  $J_{\perp}$  is AFM. (c)  $\text{Bi}_2\text{Te}_3$  structured in QLs separated by a VdW gap. (d)  $\text{VTe}_2$ .

## 2. Materials and Methods

The deposition of  $\text{VBi}_2\text{Te}_4$  is performed on (0001)- $\text{Al}_2\text{O}_3$  substrates in an ultrahigh vacuum Octoplus 300 MBE system from Dr. Eberl MBE Komponenten with a base pressure

of  $5.0 \times 10^{-11}$  mbar. High-purity (6N) bismuth (Bi) and tellurium (Te) are evaporated from standard Knudsen effusion cells and their fluxes are calibrated by a quartz crystal monitor. The Bi- and Te-flux are kept constant during the depositions at  $\phi_{\text{Bi}} = 0.0027 \text{ \AA/s}$  and  $\phi_{\text{Te}} = 0.072 \text{ \AA/s}$ .  $\phi_{\text{Te}}$  is set to a high flux to prevent Te vacancies. High-purity (5N) vanadium (V) is evaporated from a custom high-temperature Knudsen effusion cell. The flux,  $\phi_{\text{V}}$ , is indicated by the heating temperature of the Knudsen cell and is varied from 1750 °C to 1900 °C. The combination of the V-pocket size and the high evaporation temperature result in a large flux instability measured with the quartz crystal monitor, and therefore the pocket temperature will be kept as a reference for  $\phi_{\text{V}}$ . An estimate for the flux variation in this temperature range is from 0.001  $\text{\AA/s}$  to 0.0080  $\text{\AA/s}$ . The substrate temperature  $T_{\text{sub}}$  was kept constant at 150 °C. Before the deposition of  $\text{VBi}_2\text{Te}_4$ , a buffer layer of  $\text{Bi}_2\text{Te}_3$  was deposited of  $\approx 1$  nm. The samples discussed in this article are deposited using the co-evaporation method, meaning all elemental beams are opened simultaneously during the full deposition. In addition to these results, some attempts were made to use a beam-shuttering method to interrupt the V- and Bi-beams during the deposition. First, Bi and Te are opened to deposit a monolayer of  $\text{Bi}_2\text{Te}_3$ . Second, V and Te are opened to deposit a monolayer of  $\text{VTe}$  on top of the  $\text{Bi}_2\text{Te}_3$  layer. Third, an annealing step is applied during which the  $\text{VTe}$  layer should diffuse into  $\text{Bi}_2\text{Te}_3$  to form the SL of  $\text{VBi}_2\text{Te}_4$ . These three steps were repeated to form a multilayered  $\text{VBi}_2\text{Te}_4$  film. This method was previously used to successfully deposit  $\text{MnBi}_2\text{Te}_4$  by MBE [27], but for  $\text{VBi}_2\text{Te}_4$  the beam-shuttered method resulted in the same observations discussed here for the co-evaporation method showing a phase separation to  $\text{VTe}_2$  and  $\text{Bi}_2\text{Te}_3$ . Right after deposition, a RHEED image of the diffraction pattern is taken. From the RHEED image the in-plane lattice constant can be deduced by comparing the diffraction pattern of the film to a known substrate.

The crystal structure of the films is measured with XRD, STEM and EDX. The XRD measurements are performed with a Bruker D8 Discover system (Bruker, Billerica, MA, USA) with a two-dimensional Eiger2 500K detector and a two-bounce channel-cut germanium monochromator. Symmetric  $2\theta$ - $\omega$  scans were performed along the surface normal direction. The STEM measurements are made with a Thermo Scientific Spectra 300 STEM (Thermo Fisher Scientific, Waltham, MA, USA) with an electron beam voltage of 300 kV and a high-angle annular dark-field (HAADF) detector.

### 3. Results

The crystal structure of the films is analysed with STEM, EDX and XRD. STEM is performed on a sample deposited with  $\phi_{\text{V}} = 1800 \text{ }^\circ\text{C}$  (Figure 2a). The image shows the V-Bi-Te film and the  $\text{Al}_2\text{O}_3$  substrate. These STEM results clearly indicate two regions by looking at the contrast. These variations are caused by the Z-contrast related to the atomic weight of the present elements. For a V-Bi-Te sample, the atomic weights are arranged as  $m_{\text{Bi}} > m_{\text{Te}} > m_{\text{V}}$ . Therefore, the bright areas in Figure 2a are Bi-rich regions. These results clearly indicate a phase separation between a Bi-compound and a non-Bi compound. EDX (Figure 2b) shows a clear separation between a Bi/Te region and a V/Te region. Figure 2c shows a detailed STEM scan of the sample. The atoms in the bright areas are structured as a QL separated by a VdW-gap. This structure is consistent with  $\text{Bi}_2\text{Te}_3$  (Figure 1c). In the darker area the bright atoms form the typical Te octahedra of  $\text{VTe}_2$  which are separated by a VdW gap as shown in Figure 1d. The in-plane lattice constant  $a$  is related to the distance between the atoms in the x-direction,  $dx$ . Figure 2d shows the distribution of  $dx$  as extracted from Figure 2c. This distribution indicates two clearly separated regions. The in-plane lattice constants related to these two regions are calculated from the  $dx$  value with maximum intensity as  $a = 2dx$  for both  $\text{Bi}_2\text{Te}_3$  and  $\text{VTe}_2$ . This calculation results in the lattice constants  $a_1 = 3.82 \text{ \AA}$ , corresponding to  $\text{VTe}_2$ , and  $a_2 = 4.65 \text{ \AA}$ , corresponding to  $\text{Bi}_2\text{Te}_3$ .

Figure 2e presents the  $2\theta$ - $\omega$  scans of films deposited with different  $\phi_{\text{V}}$ . The peaks in the  $2\theta$ - $\omega$  scans can be identified as the (001)- $\text{Bi}_2\text{Te}_3$  and (001)- $\text{VTe}_2$  peaks. The dotted arrow at the (006)- $\text{Bi}_2\text{Te}_3$  peak indicates the dominance of  $\text{Bi}_2\text{Te}_3$  at low  $\phi_{\text{V}}$ , but the intensity of

this phase decreases as  $\phi_V$  increases. The dashed arrow at the (001)-VTe<sub>2</sub> peak indicates the dominance of VTe<sub>2</sub> at high  $\phi_V$ , but this phase disappears as  $\phi_V$  decreases. VBi<sub>2</sub>Te<sub>4</sub> is absent in all  $2\theta$ - $\omega$  scans.

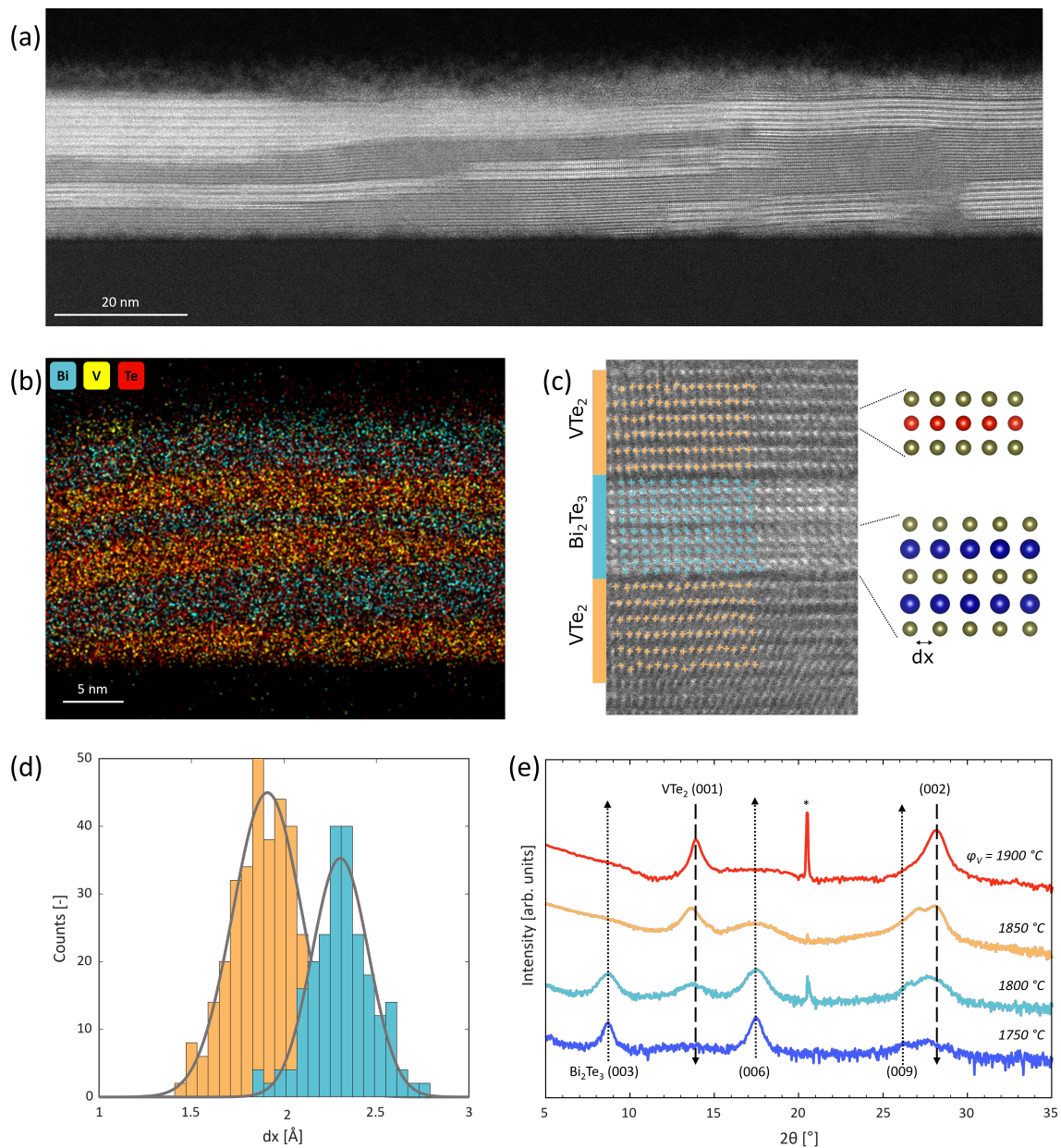


**Figure 2.** (a) STEM image of a V-Bi-Te sample. The image is taken with a HAADF detector at 300 keV. A clear phase separation between bright and dark areas can be observed. (b) EDX scan of the V-Bi-Te sample. A strong separation between V-regions and Bi-regions can be observed. (c) STEM image of a smaller region on a V-Bi-Te sample. The bright areas (blue) show the QL structure of Bi<sub>2</sub>Te<sub>3</sub> and the dark areas (orange) the VTe<sub>2</sub> structure. (d) Histogram of the atomic distance in the x-direction. (e)  $2\theta$ - $\omega$  scans indicating (001)-Bi<sub>2</sub>Te<sub>3</sub> being dominant at low  $\phi_V$ , while (001)-VTe<sub>2</sub> is dominant at high  $\phi_V$ . The arrows indicate the disappearance of the respective phases as a function of  $\phi_V$ . \* indicates the Al<sub>2</sub>O<sub>3</sub> substrate peak.

The surface of the films is analysed with RHEED and AFM. Figure 3a presents the in situ RHEED pattern of a film deposited with  $\phi_V = 1750$  °C. The RHEED pattern consists of a double streak pattern as indicated by the blue and white arrows. This doubled pattern indicates the presence of two separate crystal phases at the surface. The in-plane lattice

constants related to these streaks are  $a_1 = 4.31 \text{ \AA}$  (white arrows) and  $a_2 = 3.59 \text{ \AA}$  (blue arrows). These values correspond well with the lattice constants of  $\text{Bi}_2\text{Te}_3$  and  $\text{VTe}_2$ , respectively.

The surface morphology is measured by AFM. Figure 3b shows the height distribution as measured with AFM for films deposited with different  $\phi_V$ . The insets show the surface morphology of the films with  $\phi_V = 1750 \text{ }^\circ\text{C}$  and  $\phi_V = 1900 \text{ }^\circ\text{C}$ . At low  $\phi_V$ , the morphology shows strong island formation and the triangular crystals typically observed for  $\text{Bi}_2\text{Te}_3$ . The results at high  $\phi_V$  show a relative flat film without any sharp crystals. The height distributions indicate a strong influence of the  $\phi_V$  on the distribution spread. With an increasing  $\phi_V$ , the height variation becomes smaller, indicating a flatter surface.

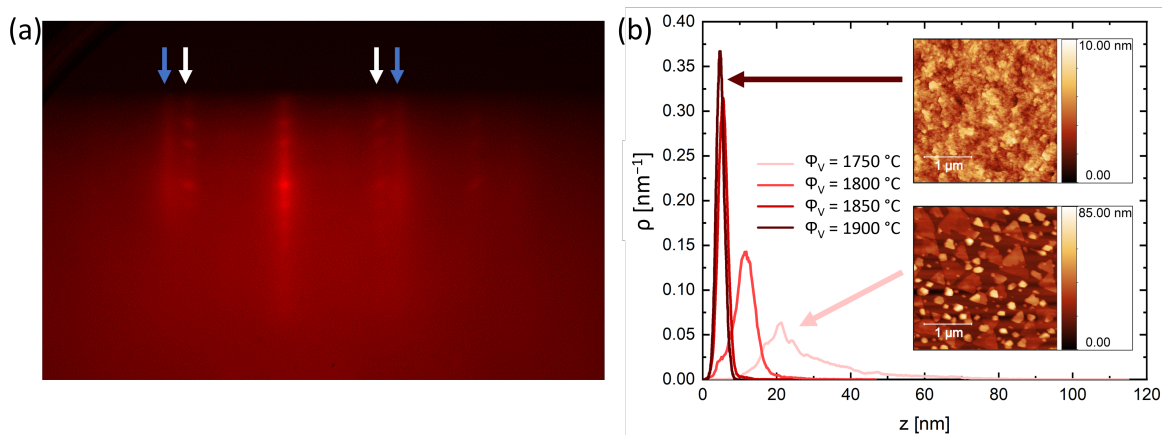


**Figure 3.** (a) RHEED pattern for  $\phi_V = 1750 \text{ }^\circ\text{C}$  showing a double streak pattern related to the phases  $\text{Bi}_2\text{Te}_3$  with  $a_1 = 4.31 \text{ \AA}$  and  $\text{VTe}_2$  with  $a_2 = 3.59 \text{ \AA}$ , indicated by the blue and white arrows, respectively. (b) Height distribution at the surface as a function of the  $\phi_V$ . The insets show the surface morphology of the samples with  $\phi_V = 1750 \text{ }^\circ\text{C}$  and  $\phi_V = 1900 \text{ }^\circ\text{C}$ .

#### 4. Discussion

$\text{VBi}_2\text{Te}_4$  is a SL structure requiring the embedding of  $\text{VTe}$  within the QL structure of  $\text{Bi}_2\text{Te}_3$ . According to our results, the formation of  $\text{VBi}_2\text{Te}_4$  is unstable with respect to phase separated  $\text{Bi}_2\text{Te}_3$  and  $\text{VTe}_2$  within the thermodynamic conditions of the MBE. The instability of  $\text{VBi}_2\text{Te}_4$  can have various causes.

First, a large in-plane lattice mismatch,  $\Delta_a$ , between  $\text{VTe}_2$  and  $\text{Bi}_2\text{Te}_3$  might prohibit the formation of  $\text{VBi}_2\text{Te}_4$  [28]. Our STEM results indicate  $\Delta_a = 0.83 \text{ \AA}$  between the two phases. The theoretically predicted lattice constant of  $\text{VBi}_2\text{Te}_4$ ,  $a = 4.37 \text{ \AA}$ , is close to the lattice constant of  $\text{Bi}_2\text{Te}_3$ ,  $a = 4.65 \text{ \AA}$ . Therefore, the  $\text{VTe}_2$  lattice has to overcome  $\Delta_a$  to form  $\text{VBi}_2\text{Te}_4$ . Table 1 gives an overview of different materials structured as a SL with the relevant lattice constants and whether the material was successfully observed in experiments. The intercalated layer is presented as  $\text{XTe}$  or  $\text{XTe}_2$ , depending on the experimental stability of the phases. The experimentally successful materials match  $\Delta_a < 0.6 \text{ \AA}$ , while the experimentally unsuccessful materials match  $\Delta_a > 0.5 \text{ \AA}$ . This difference can indicate a limit to the maximum allowed  $\Delta_a$  of  $0.5 \text{ \AA}$  to  $0.6 \text{ \AA}$  between the SL material and the intercalated layer, possibly explaining the phase separation in  $\text{VBi}_2\text{Te}_4$ . However, this observation does not match with the stability of  $\text{PbBi}_2\text{Te}_4$  and  $\text{SnBi}_2\text{Te}_4$  [29]. Therefore, the lattice mismatch between the intercalated layer and  $\text{Bi}_2\text{Te}_3$  does not completely explain the instability of the SL structure in general, and another factor should be considered.

Second, the elemental valence states in the intercalated layer might prohibit the formation of the SL. In the SL, the preferred valence states are  $\text{M}^{(+2)}\text{Bi}_2^{(+3)}\text{Te}_4^{(-2)}$  ( $\text{M}$  = transition metal or rare-earth element), which matches well with the valence states of an intercalated layer structure of  $\text{M}^{(+2)}\text{Te}^{(-2)}$  [30]. However, when the stable compound of the intercalated layer is structured as  $\text{M}^{(+4)}\text{Te}_2^{(-2)}$  the valence states of the intercalated layer and the SL do not match. A mismatch between the preferred valence state of the intercalated layer and the SL indicates the instability of the SL. Table 1 reflects this instability, showing that every

experimentally observed intercalated layer bulk compound with a valence structure of  $M^{(+2)}Te^{(-2)}$  also has a stable SL counterpart, but a valence structure of  $M^{(+4)}Te_2^{(-2)}$  does not. This is in agreement with our study on  $VBi_2Te_4$ , because  $VTe_2$  is thermodynamically more stable than  $VTe$  [31].

Furthermore, ref. [32] studied the preferred valence states of V, Cr, Mn and Fe in  $Bi_2Te_3$ . In Te-rich conditions, only  $V^{3+}$  and  $Cr^{3+}$  can substitute neutrally for  $Bi^{3+}$  atoms in  $Bi_2Te_3$ . In contrast, Mn and Fe mostly form  $Mn^{2+}$  and  $Fe^{2+}$ , which create energetically unfavourable states when mixed with  $Bi^{3+}$  [9,32]. This additionally shows the unfavourable  $V^{2+}$  valence state. Therefore, Mn and Fe can more easily form a neutral SL structure with respect to V and Cr.

**Table 1.** Overview of materials with a unit cell structured as a SL. The table presents whether the material is successfully synthesised experimentally, the lattice constants found in the literature for these materials (either experimental or theoretical values), the intercalated layer with the corresponding lattice constant and the lattice mismatch between the SL and the intercalated layer. The intercalated layer is presented as  $XTe$  or  $XTe_2$ , depending on the experimental stability of the phases.

Material	Experimentally Observed?	$a_{SL}$ [Å]	Intercalated Layer	$a_{int}$ [Å]	Lattice Structure	$\Delta_a$ [Å]
$VBi_2Te_4$	No	4.34–4.37 [9,26,33–35]	$VTe_2$	3.59	Hexagonal, $P\bar{3}m1$	0.75–0.78
$MnBi_2Te_4$	Yes [8,21–23,27,36]	4.33 [36]	$MnTe$	4.13 [37]	Hexagonal, $P6_3/mmc$	0.20
$FeBi_2Te_4$	Yes [38]	4.39 [9,38]	$FeTe$	3.83 [38,39]	Tetragonal, $P4/nmm$	0.56
$EuBi_2Te_4$	No	4.50 [9,33]	$FeTe_2$	3.77 [40]	Hexagonal, $P\bar{3}m1$	0.63
			$EuTe$	6.60 [41,42]	Cubic, $Fm\bar{3}m$	2.10
			$EuTe_2$	6.97 [43]	Tetragonal, $I4/mcm$	2.47
$NiBi_2Te_4$	Yes *	4.30 [9,33]	$NiTe_2$	3.86 [44]	Hexagonal, $P\bar{3}m1$	0.44
$CrBi_2Te_4$	No	4.32 [45]	$CrTe_2$	3.79 [46]	Hexagonal, $P\bar{3}m1$	0.53
$TiBi_2Te_4$	No	4.39 [9]	$TiTe_2$	3.78 [47]	Hexagonal, $P\bar{3}m1$	0.61
$PbBi_2Te_4$	Yes [48,49]	4.44 [49]	$PbTe$	6.46 [50]	Cubic, $Fm\bar{3}m$	2.02
$SnBi_2Te_4$	Yes [51–53]	4.40 [51,53]	$SnTe$	6.32 [50]	Cubic, $Fm\bar{3}m$	1.92
$GeBi_2Te_4$	Yes [54,55]	4.33 [54,55]	$GeTe$	4.16 [50,56]	Rhombohedral, $R\bar{3}m$	0.17

\* Not observed as multilayered/bulk material. Ref. [57] observed the SL structure as an intercalated layer between  $Bi_2Te_3$  and Ni-doped  $Bi_2Te_3$ .

In conclusion, the influence of the  $\phi_V$  during MBE depositions was investigated on the synthesis of the  $VBi_2Te_4$  phase. The resulting films do not show any indication of  $VBi_2Te_4$  but rather a phase separation into  $Bi_2Te_3$  and  $VTe_2$ . These results show  $VBi_2Te_4$  is unstable within the deposition conditions of MBE.

**Author Contributions:** Conceptualization, T.J. and A.B.; methodology, M.A. and T.J.; validation, M.A. and T.J.; formal analysis, M.A., T.J. and M.T.; investigation, M.A. and T.J.; resources, M.T. and A.B.; data curation, M.A., T.J. and A.B.; writing—original draft preparation, M.A.; writing—review and editing, M.A., T.J., M.T. and A.B.; visualization, M.A. and T.J.; supervision, A.B.; project administration, M.A. and T.J.; funding acquisition, A.B. All authors have read and agreed to the published version of the manuscript.

**Funding:** This research was funded by the research program “Materials for the Quantum Age” (QuMat) and the Dutch Research Council (NWO). QuMat (registration number 024.005.006) is part of the Gravitation program financed by the Dutch Ministry of Education, Culture and Science (OCW). The NWO supports this research via the TOPCORE project (registration number OCENW.GROOT.2019.048).

**Data Availability Statement:** The data presented in this study are openly available in 4TU.ResearchData at 10.4121/95ee6f7b-3cf7-4c01-a461-860e6f9485bf.

**Acknowledgments:** We would like to acknowledge Daan Wielens and Frank Roesthuis for technical support and Anna Isaeva for sharing her expertise on the synthesis of septuple-layered materials.

**Conflicts of Interest:** The authors declare no conflicts of interest.

## References

1. Hasan, M.Z.; Kane, C.L. Colloquium: Topological insulators. *Rev. Mod. Phys.* **2010**, *82*, 3045–3067. [[CrossRef](#)]
2. Yu, R.; Zhang, W.; Zhang, H.J.; Zhang, S.C.; Dai, X.; Fang, Z. Quantized anomalous Hall effect in magnetic topological insulators. *Science* **2010**, *329*, 61–64. [[CrossRef](#)]
3. Liu, C.X.; Qi, X.L.; Dai, X.; Fang, Z.; Zhang, S.C. Quantum anomalous Hall effect in  $\text{Hg}_{1-y}\text{Mn}_y\text{Te}$  quantum wells. *Phys. Rev. Lett.* **2008**, *101*, 146802. [[CrossRef](#)] [[PubMed](#)]
4. Liu, Q.; Liu, C.X.; Xu, C.; Qi, X.L.; Zhang, S.C. Magnetic impurities on the surface of a topological insulator. *Phys. Rev. Lett.* **2009**, *102*, 156603. [[CrossRef](#)] [[PubMed](#)]
5. Haldane, F.D.M. Model for a quantum Hall effect without Landau levels: Condensed-matter realization of the “parity anomaly”. *Phys. Rev. Lett.* **1988**, *61*, 2015–2018. [[CrossRef](#)] [[PubMed](#)]
6. Chang, C.Z.; Zhang, J.; Feng, X.; Shen, J.; Zhang, Z.; Guo, M.; Ou, Y.; Wei, P.; Jun, L.; Ji, Z.; et al. Experimental observation of the quantum anomalous Hall effect in a magnetic topological insulator. *Science* **2013**, *340*, 167–170. [[CrossRef](#)] [[PubMed](#)]
7. Chang, C.Z.; Zhao, W.; Kim, D.Y.; Zhang, H.; Assaf, B.A.; Heiman, D.; Zhang, S.C.; Liu, C.; Chan, M.H.W.; Moodera, J.S. High-precision realization of robust quantum anomalous Hall state in a hard ferromagnetic topological insulator. *Nat. Mater.* **2015**, *14*, 473–477. [[CrossRef](#)] [[PubMed](#)]
8. Deng, Y.; Yu, Y.; Shi, M.Z.; Guo, Z.; Xu, Z.; Wang, J.; Chen, X.H.; Zhang, Y. Quantum anomalous Hall effect in intrinsic magnetic topological insulator  $\text{MnBi}_2\text{Te}_4$ . *Science* **2020**, *367*, 895–900. [[CrossRef](#)]
9. Li, J.; Li, Y.; Du, S.; Wang, Z.; Gu, B.L.; Zhang, S.C.; He, K.; Duan, W.; Xu, Y. Intrinsic magnetic topological insulators in van der Waals layered  $\text{MnBi}_2\text{Te}_4$ -family materials. *Sci. Adv.* **2019**, *5*, eaaw5685. [[CrossRef](#)]
10. Watanabe, R.; Yoshimi, R.; Kawamura, M.; Mogi, M.; Tsukazaki, A.; Yu, X.Z.; Nakajima, K.; Takahashi, K.S.; Kawasaki, M.; Tokura, Y. Quantum anomalous Hall effect driven by magnetic proximity coupling in all-telluride based heterostructure. *Appl. Phys. Lett.* **2019**, *115*, 102403. [[CrossRef](#)]
11. Ou, Y.; Liu, C.; Jiang, G.; Feng, Y.; Zhao, D.; Wu, W.; Wang, X.X.; Li, W.; Song, C.; Wang, L.L.; et al. Enhancing the quantum anomalous Hall effect by magnetic codoping in a topological insulator. *Adv. Mater.* **2018**, *30*, 1703062. [[CrossRef](#)]
12. Qi, X.L.; Hughes, T.L.; Zhang, S.C. Topological field theory of time-reversal invariant insulators. *Phys. Rev. B* **2008**, *78*, 195424. [[CrossRef](#)]
13. Li, R.; Wang, J.; Qi, X.L.; Zhang, S.C. Dynamical axion field in topological magnetic insulators. *Nat. Phys.* **2010**, *6*, 284–288. [[CrossRef](#)]
14. Wang, P.; Ge, J.; Li, J.; Liu, Y.; Xu, Y.; Wang, J. Intrinsic magnetic topological insulators. *Innovation* **2021**, *2*, 100098. [[CrossRef](#)] [[PubMed](#)]
15. Mogi, M.; Kawamura, M.; Yoshimi, R.; Tsukazaki, A.; Kozuka, Y.; Shirakawa, N.; Takahashi, K.S.; Kawasaki, M.; Tokura, Y. A magnetic heterostructure of topological insulators as a candidate for an axion insulator. *Nat. Mater.* **2017**, *16*, 516–521. [[CrossRef](#)] [[PubMed](#)]
16. Grutter, A.J.; He, Q.L. Magnetic proximity effects in topological insulator heterostructures: Implementation and characterization. *Phys. Rev. Mater.* **2021**, *5*, 090301. [[CrossRef](#)]
17. Hor, Y.S.; Roushan, P.; Beidenkopf, H.; Seo, J.; Qu, D.; Checkelsky, J.G.; Wray, L.A.; Hsieh, D.; Xia, Y.; Xu, S.Y.; et al. Development of ferromagnetism in the doped topological insulator  $\text{Bi}_{2-x}\text{Mn}_x\text{Te}_3$ . *Phys. Rev. B* **2010**, *81*, 195203. [[CrossRef](#)]
18. Katmis, F.; Lauter, V.; Nogueira, F.S.; Assaf, B.A.; Jamer, M.E.; Wei, P.; Satpati, B.; Freeland, J.W.; Eremin, I.; Heiman, D.; et al. A high-temperature ferromagnetic topological insulating phase by proximity coupling. *Nature* **2016**, *533*, 513–516. [[CrossRef](#)] [[PubMed](#)]
19. Tang, C.; Chang, C.Z.; Zhao, G.; Liu, Y.; Jiang, Z.; Liu, C.X.; McCartney, M.R.; Smith, D.J.; Chen, T.; Moodera, J.S.; et al. Above 400-K robust perpendicular ferromagnetic phase in a topological insulator. *Sci. Adv.* **2017**, *3*, e1700307. [[CrossRef](#)]
20. He, Q.L.; Yin, G.; Yu, L.; Grutter, A.J.; Pan, L.; Chen, C.Z.; Che, X.; Yu, G.; Zhang, B.; Shao, Q.; et al. Topological transitions induced by antiferromagnetism in a thin-film topological insulator. *Phys. Rev. Lett.* **2018**, *121*, 096802. [[CrossRef](#)]
21. Rienks, E.D.L.; Wimmer, S.; Sánchez-Barriga, J.; Caha, O.; Mandal, P.S.; Růžička, J.; Ney, A.; Steiner, H.; Volobuev, V.V.; Groiss, H.; et al. Large magnetic gap at the Dirac point in  $\text{Bi}_2\text{Te}_3/\text{MnBi}_2\text{Te}_4$  heterostructures. *Nature* **2019**, *576*, 423–428. [[CrossRef](#)] [[PubMed](#)]
22. Liu, C.; Wang, Y.; Li, H.; Wu, Y.; Li, Y.; Li, J.; He, K.; Xu, Y.; Zhang, J.; Wang, Y. Robust axion insulator and Chern insulator phases in a two-dimensional antiferromagnetic topological insulator. *Nat. Mater.* **2020**, *19*, 522–527. [[CrossRef](#)] [[PubMed](#)]
23. Otrokov, M.M.; Klimovskikh, I.I.; Bentmann, H.; Estyunin, D.; Zeugner, A.; Aliev, Z.S.; Gaß, S.; Wolter, A.U.B.; Koroleva, A.V.; Shikin, A.M.; et al. Prediction and observation of an antiferromagnetic topological insulator. *Nature* **2019**, *576*, 416–422. [[CrossRef](#)]

24. Otrokov, M.M.; Rusinov, I.P.; Blanco-Rey, M.; Hoffmann, M.; Vyazovskaya, A.Y.; Ereemeev, S.V.; Ernst, A.; Echenique, P.M.; Arnau, A.; Chulkov, E.V. Unique thickness-dependent properties of the van der Waals interlayer antiferromagnet  $\text{MnBi}_2\text{Te}_4$  films. *Phys. Rev. Lett.* **2019**, *122*, 107202. [[CrossRef](#)] [[PubMed](#)]
25. Zhang, D.; Shi, M.; Zhu, T.; Xing, D.; Zhang, H.; Wang, J. Topological axion states in the magnetic insulator  $\text{MnBi}_2\text{Te}_4$  with the quantized magnetoelectric effect. *Phys. Rev. Lett.* **2019**, *122*, 206401. [[CrossRef](#)]
26. Petrov, E.K.; Men'shov, V.N.; Rusinov, I.P.; Hoffmann, M.; Ernst, A.; Otrokov, M.M.; Dugaev, V.K.; Menshchikova, T.V.; Chulkov, E.V. Domain wall induced spin-polarized flat bands in antiferromagnetic topological insulators. *Phys. Rev. B* **2021**, *103*, 235142. [[CrossRef](#)]
27. Gong, Y.; Guo, J.; Li, J.; Zhu, K.; Liao, M.; Liu, X.; Zhang, Q.; Gu, L.; Tang, L.; Feng, X.; et al. Experimental realization of an intrinsic magnetic topological insulator. *Chin. Phys. Lett.* **2019**, *36*, 076801. [[CrossRef](#)]
28. Jiao, F.; Wang, J.; Wang, X.; Tian, Q.; Chang, M.; Cai, L.; Zhu, S.; Zhang, D.; Lu, Q.; Wang, C.; et al. The Layer-Inserting Growth of Antiferromagnetic Topological Insulator  $\text{MnBi}_2\text{Te}_4$  Based on Symmetry and Its X-ray Photoelectron Spectroscopy. *J. Supercond. Nov. Magn.* **2021**, *34*, 1485–1493. [[CrossRef](#)]
29. Sans, J.A.; Vilaplana, R.; da Silva, E.L.; Popescu, C.; Cuenca-Gotor, V.P.; Andrada-Chacón, A.; Sánchez-Benitez, J.; Gomis, O.; Pereira, A.L.J.; Rodríguez-Hernández, P.; et al. Characterization and Decomposition of the Natural van der Waals  $\text{SnSb}_2\text{Te}_4$  under Compression. *Inorg. Chem.* **2020**, *59*, 9900–9918. [[CrossRef](#)]
30. Zeugner, A.; Nietschke, F.; Wolter, A.U.B.; Gaß, S.; Vidal, R.C.; Peixoto, T.R.F.; Pohl, D.; Damm, C.; Lubk, A.; Hentrich, R.; et al. Chemical Aspects of the Candidate Antiferromagnetic Topological Insulator  $\text{MnBi}_2\text{Te}_4$ . *Chem. Mater.* **2019**, *31*, 2795–2806. [[CrossRef](#)]
31. Parker, D.S.; Yin, L.; Samolyuk, G.D.; Sanjeeva, L.D.; Wang, X.; Cooper, V.R.; Liu, Y.; Bud'ko, S.; Sefat, A.S. Insulating antiferromagnetism in VTe. *Phys. Rev. B* **2022**, *105*, 174414. [[CrossRef](#)]
32. Zhang, J.M.; Ming, W.; Huang, Z.; Liu, G.B.; Kou, X.; Fan, Y.; Wang, K.L.; Yao, Y. Stability, electronic, and magnetic properties of the magnetically doped topological insulators  $\text{Bi}_2\text{Se}_3$ ,  $\text{Bi}_2\text{Te}_3$ , and  $\text{Sb}_2\text{Te}_3$ . *Phys. Rev. B* **2013**, *88*, 235131. [[CrossRef](#)]
33. Li, Z.; Li, J.; He, K.; Wan, X.; Duan, W.; Xu, Y. Tunable interlayer magnetism and band topology in van der Waals heterostructures of  $\text{MnBi}_2\text{Te}_4$ -family materials. *Phys. Rev. B* **2020**, *102*, 081107. [[CrossRef](#)]
34. Zhang, Y.; Wang, Y.; Yang, W.; Zhang, H.; Jia, J. Strain-tunable magnetism and topological states in layered  $\text{VBi}_2\text{Te}_4$ . *Phys. Chem. Chem. Phys.* **2023**, *25*, 28189–28195. [[CrossRef](#)] [[PubMed](#)]
35. Zhu, W.; Song, C.; Liao, L.; Zhou, Z.; Bai, H.; Zhou, Y.; Pan, F. Quantum anomalous Hall insulator state in ferromagnetically ordered  $\text{MnBi}_2\text{Te}_4/\text{VBi}_2\text{Te}_4$  heterostructures. *Phys. Rev. B* **2020**, *102*, 085111. [[CrossRef](#)]
36. Lee, D.S.; Kim, T.H.; Park, C.H.; Chung, C.Y.; Lim, Y.S.; Seo, W.S.; Park, H.H. Crystal structure, properties and nanostructuring of a new layered chalcogenide semiconductor,  $\text{Bi}_2\text{MnTe}_4$ . *CrystEngComm* **2013**, *15*, 5532–5538. [[CrossRef](#)]
37. Kriegner, D.; Reichlova, H.; Grenzer, J.; Schmidt, W.; Ressouche, E.; Godinho, J.; Wagner, T.; Martin, S.Y.; Shick, A.B.; Volobuev, V.V.; et al. Magnetic anisotropy in antiferromagnetic hexagonal MnTe. *Phys. Rev. B* **2017**, *96*, 214418. [[CrossRef](#)]
38. Saxena, A.; Rani, P.; Nagpal, V.; Patnaik, S.; Felner, I.; Awana, V.P.S. Crystal growth and characterization of possible new magnetic topological insulators  $\text{FeBi}_2\text{Te}_4$ . *J. Supercond. Nov. Magn.* **2020**, *33*, 2251–2256. [[CrossRef](#)]
39. Oyler, K.D.; Ke, X.; Sines, I.T.; Schiffer, P.; Schaak, R.E. Chemical Synthesis of Two-Dimensional Iron Chalcogenide Nanosheets:  $\text{FeSe}$ ,  $\text{FeTe}$ ,  $\text{Fe}(\text{Se},\text{Te})$ , and  $\text{FeTe}_2$ . *Chem. Mater.* **2009**, *21*, 3655–3661. [[CrossRef](#)]
40. Wu, H.; Feng, Z.; Pal, A.; Dong, H.; Jing, C.; Wang, K.; Zhang, S.; Deng, W.; Li, S.; Feng, J.; et al. Evolution of Temperature-Induced Isostructural Phase Transition in a Newly Grown Layered  $\text{FeTe}_2$  Single Crystal. *Chem. Mater.* **2021**, *33*, 4927–4935. [[CrossRef](#)]
41. Radomska, A.; Balcerzak, T. Calculations of  $\text{EuTe}$  magnetic phase diagram for external pressure. *Acta Phys. Pol. A* **2000**, *98*, 83–91. [[CrossRef](#)]
42. Fornari, C.I.; Bentmann, H.; Morelhão, S.L.; Peixoto, T.R.F.; Rapp, P.H.O.; Tcakaev, A.V.; Zabolotnyy, V.; Kamp, M.; Lee, T.L.; Min, C.H.; et al. Incorporation of Europium in  $\text{Bi}_2\text{Te}_3$  topological insulator epitaxial films. *J. Phys. Chem. C* **2020**, *124*, 16048–16057. [[CrossRef](#)]
43. Yin, J.; Wu, C.; Li, L.; Yu, J.; Sun, H.; Shen, B.; Frandsen, B.A.; Yao, D.X.; Wang, M. Large negative magnetoresistance in the antiferromagnetic rare-earth dichalcogenide  $\text{EuTe}_2$ . *Phys. Rev. Mater.* **2020**, *4*, 013405. [[CrossRef](#)]
44. Xu, C.; Li, B.; Jiao, W.; Zhou, W.; Qian, B.; Sankar, R.; Zhigadlo, N.D.; Qi, Y.; Qian, D.; Chou, F.C.; et al. Topological type-II Dirac fermions approaching the Fermi level in a transition metal dichalcogenide  $\text{NiTe}_2$ . *Chem. Mater.* **2018**, *30*, 4823–4830. [[CrossRef](#)]
45. Petrov, E.K.; Ernst, A.; Menshchikova, T.V.; Chulkov, E.V. Intrinsic magnetic topological insulator state induced by the Jahn–Teller effect. *J. Phys. Chem. Lett.* **2021**, *12*, 9076–9085. [[CrossRef](#)] [[PubMed](#)]
46. Freitas, D.C.; Weht, R.; Sulpice, A.; Remenyi, G.; Strobel, P.; Gay, F.; Marcus, J.; Núñez-Regueiro, M. Ferromagnetism in layered metastable  $1\text{T-CrTe}_2$ . *J. Phys. Condens. Matter* **2015**, *27*, 176002. [[CrossRef](#)] [[PubMed](#)]
47. Chen, P.; Pai, W.W.; Chan, Y.H.; Takayama, A.; Xu, C.Z.; Karn, A.; Hasegawa, S.; Chou, M.Y.; Mo, S.K.; Fedorov, A.V.; et al. Emergence of charge density waves and a pseudogap in single-layer  $\text{TiTe}_2$ . *Nat. Commun.* **2017**, *8*, 516. [[CrossRef](#)]
48. Kuroda, K.; Miyahara, H.; Ye, M.; Ereemeev, S.V.; Koroteev, Y.M.; Krasovskii, E.E.; Chulkov, E.V.; Hiramoto, S.; Moriyoshi, C.; Kuroiwa, Y.; et al. Experimental verification of  $\text{PbBi}_2\text{Te}_4$  as a 3D topological insulator. *Phys. Rev. Lett.* **2012**, *108*, 206803. [[CrossRef](#)]
49. Xu, X.; Ni, D.; Xie, W.; Cava, R.J. Superconductivity in electron-doped  $\text{PbBi}_2\text{Te}_4$ . *Phys. Rev. B* **2023**, *108*, 054525. [[CrossRef](#)]

50. Bauer Pereira, P.; Sergueev, I.; Gorsse, S.; Dadda, J.; Müller, E.; Hermann, R.P. Lattice dynamics and structure of GeTe, SnTe and PbTe. *Phys. Status Solidi (B)* **2013**, *250*, 1300–1307. [[CrossRef](#)]
51. Saxena, A.; Karn, N.K.; Sharma, M.M.; Awana, V.P.S. Detailed structural and topological analysis of SnBi<sub>2</sub>Te<sub>4</sub> single crystal. *J. Phys. Chem. Solids* **2023**, *174*, 111169. [[CrossRef](#)]
52. Zou, Y.C.; Chen, Z.G.; Zhang, E.; Kong, F.; Lu, Y.; Wang, L.; Drennan, J.; Wang, Z.; Xiu, F.; Cho, K.; et al. Atomic disorders in layer structured topological insulator SnBi<sub>2</sub>Te<sub>4</sub> nanoplates. *Nano Res.* **2018**, *11*, 696–706. [[CrossRef](#)]
53. Vilaplana, R.; Sans, J.A.; Manjón, F.J.; Andrada-Chacón, A.; Sánchez-Benítez, J.; Popescu, C.; Gomis, O.; Pereira, A.L.J.; García-Domene, B.; Rodríguez-Hernández, P.; et al. Structural and electrical study of the topological insulator SnBi<sub>2</sub>Te<sub>4</sub> at high pressure. *J. Alloys Compd.* **2016**, *685*, 962–970. [[CrossRef](#)]
54. Marcinkova, A.; Wang, J.K.; Slavonic, C.; Nevidomskyy, A.H.; Kelly, K.F.; Filinchuk, Y.; Morosan, E. Topological metal behavior in GeBi<sub>2</sub>Te<sub>4</sub> single crystals. *Phys. Rev. B* **2013**, *88*, 165128. [[CrossRef](#)]
55. Frolov, A.S.; Usachov, D.Y.; Tarasov, A.V.; Fedorov, A.V.; Bokai, K.A.; Klimovskikh, I.; Stolyarov, V.S.; Sergeev, A.I.; Lavrov, A.N.; Golyashov, V.A.; et al. Magnetic Dirac semimetal state of (Mn,Ge)Bi<sub>2</sub>Te<sub>4</sub>. *arXiv* **2023**, arXiv:2306.13024.
56. Serrano-Sánchez, F.; Funes, M.; Nemes, N.M.; Dura, O.J.; Martínez, J.L.; Prado-Gonjal, J.; Fernández-Díaz, M.T.; Alonso, J.A. Low lattice thermal conductivity in arc-melted GeTe with Ge-deficient crystal structure. *Appl. Phys. Lett.* **2018**, *113*, 083902. [[CrossRef](#)]
57. Bhattacharjee, N.; Mahalingam, K.; Fedorko, A.; Lauter, V.; Matzelle, M.; Singh, B.; Grutter, A.; Will-Cole, A.; Page, M.; McConney, M.; et al. Topological antiferromagnetic Van der Waals phase in topological insulator/ferromagnet heterostructures synthesized by a CMOS-compatible sputtering technique. *Adv. Mater.* **2022**, *34*, 2108790. [[CrossRef](#)] [[PubMed](#)]

**Disclaimer/Publisher’s Note:** The statements, opinions and data contained in all publications are solely those of the individual author(s) and contributor(s) and not of MDPI and/or the editor(s). MDPI and/or the editor(s) disclaim responsibility for any injury to people or property resulting from any ideas, methods, instructions or products referred to in the content.